Imaging of 180° ferroelectric domain walls in uniaxial ferroelectrics by confocal Raman spectroscopy: Unraveling the contrast mechanism

M. Rüsing,[1,2,*] S. Neufeld,[1] J. Brockmeier,[1] C. Eigner,[1] P. Mackwitz,[1] K. Spychala,[1] C. Silberhorn,[1] W. G. Schmidt,[1] G. Berth,[1] A. Zrenner,[1] and S. Sanna[3]

[1]*Department Physik, Universität Paderborn, 33095 Paderborn, Germany*

[2]*Department of Electrical and Computer Engineering, University of California, San Diego, 9500 Gilman Dr, La Jolla, California 92093, USA*

[3]*Institut für Theoretische Physik, Justus-Liebig-Universität Gießen, 35392 Gießen, Germany*

(Received 26 May 2018; revised manuscript received 23 July 2018; published 12 October 2018)

In recent years, Raman spectroscopy has been used to visualize and analyze ferroelectric domain structures. The technique makes use of the fact that the intensity or frequency of certain phonons is strongly influenced by the presence of domain walls. Although the method is used frequently, the underlying mechanism responsible for the changes in the spectra is not fully understood. This inhibits deeper analysis of domain structures based on this method. Two different models have been proposed. However, neither model completely explains all observations. In this work, we have systematically investigated domain walls in different scattering geometries with Raman spectroscopy in the common ferroelectric materials used in integrated optics, i.e., $KTiOPO_4$, $LiNbO_3$, and $LiTaO_3$. Based on the two models, we can demonstrate that the observed contrast for domain walls is in fact based on two different effects. We can identify on the one hand microscopic changes at the domain wall, e.g., strain and electric fields, and on the other hand a macroscopic change of selection rules at the domain wall. While the macroscopic relaxation of selection rules can be explained by the directional dispersion of the phonons in agreement with previous propositions, the microscopic changes can be explained qualitatively in terms of a simplified atomistic model.

DOI: 10.1103/PhysRevMaterials.2.103801

I. INTRODUCTION

In the last decade, Raman microscopy has been applied to visualize and analyze ferroelectric domain structures in numerous materials [1–16]. A relation between the phonon spectra and ferroelectric domain walls (DW) was first noted by Dierolf *et al.* in 2004 [1] performing luminescence microscopy on periodically poled, Er-doped lithium niobate. Since then, this method has seen widespread use for the investigation of domain walls, in particular in lithium niobate ($LiNbO_3$, LN) and lithium tantalate ($LiTaO_3$, LT). This method makes use of the fact that the intensity, and to a lesser extent the frequency or full width at half-maximum (FWHM), of certain Raman modes is heavily influenced by the presence of domain walls (DWs). These intensity variations can then be mapped to create an image of the domain structure. Raman spectroscopy is noninvasive and offers a three-dimensional resolution in confocal application. The resolution of diffraction limited microscopy (≈500 nm) is not sufficient to analyze the scale of the ferroelectric DW transition itself, which is supposed to be a few unit cells (≈1 nm) [17–21]. However, Raman spectroscopy is sensitive to other effects as well, such as crystallographic defects [7,16,22], stoichiometry [22,23], strains [24–26], or E fields [27]. The understanding of those effects and their interaction with domain structures is particular important in technological relevant systems, such as periodically poled waveguide structures [2,8,74]. This makes Raman spectroscopy a valuable tool to supplement traditional high-resolution methods to study ferroelectric domain structures, such as transition electron microscopy or piezoresponse force microscopy (PFM). Despite the widespread usage of Raman microscopy for imaging of ferroelectric domain walls, the mechanism leading to a changed phonon spectrum at the DW is not entirely understood. An understanding of the underlying contrast mechanism may allow for a better understanding of the DW transition, similar to second harmonic (SH) microscopy, where an understanding of the contrast mechanism led to the observation of theoretically predicted non-Ising ferroelectric domain transition in $LiTaO_3$ [56].

Two different models have been proposed to explain the origin of the contrast. The first explanation for the contrast was given by Fontana *et al.* [4] shortly after the first observations of DWs with Raman microscopy were made. In the years preceding the first Raman experiments on ferroelectric domain walls, large strain fields in the vicinity of domain walls in $LiNbO_3$ and $LiTaO_3$ have been observed [28,29], as well as predicted theoretically [30]. Furthermore, luminescence mapping experiment revealed large electric fields along domain walls [1,9]. Based on these observations, Fontana *et al.* suggest that these strain fields and/or the local electric fields will lead to changed Raman scattering efficiency, which they refer to as elasto-optic and electro-optic coupling. In the classical theory, the Raman intensity of a certain normal mode n is associated with the polarizability change $d\alpha/dQ^n$ with respect to the normal coordinates Q^n of the vibration [31,32]. Fontana *et al.* demonstrated that strain ds and local electric field dE will lead to additional terms in the polarizability

*mruesing@eng.ucsd.de

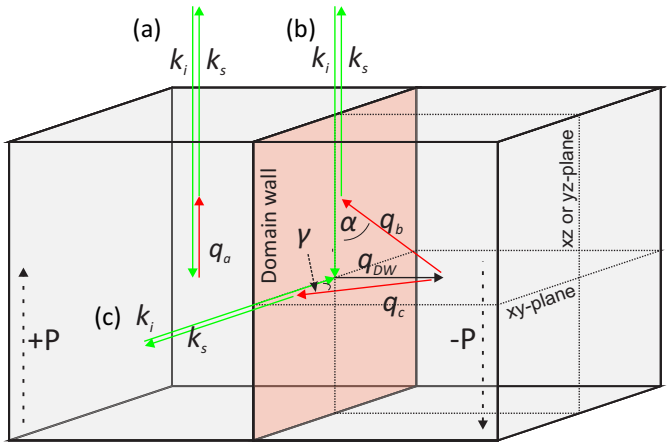

FIG. 1. Contrast mechanism as proposed by Stone and Dierolf [6]. In their model, they understand the DW as a large planar defect associated with a quasimomentum q_{DW}. This leads to a change in momentum conservation of the scattering at DWs giving rise to changes in the Raman spectrum.

change. The total polarizability including strain and electric fields is then given by Fontana *et al.* as [4]

$$\frac{d\alpha_{ij}}{dQ^n} = \frac{d\alpha_{ij}}{dQ^n} + \left(\frac{\partial\alpha_{ij}}{\partial s_{lm}} ds_{lm} + \frac{\partial\alpha_{ij}}{\partial E_k} dE_k\right) \frac{1}{dQ^n}. \quad (1)$$

This model presents a reasonable explanation to the contrast as well as the typical lengths scales of DW responses in Raman spectroscopy taking the aforementioned existence of fields and strain into account [1,9,28,29].

A different explanation for the origin of the contrast in Raman spectroscopy was presented by Stone and Dierolf [6]. In their model they understand the domain wall as an extended, planar defect. Planar defects are associated with a quasimomentum q_{DW} normal to the defect plane, as shown in Fig. 1. This will change the momentum conservation in certain scattering processes in the vicinity of DWs. In particular, oblique-propagating phonons, usually with mixed LO-TO character, can participate in the scattering process, which otherwise are forbidden in the usual backscattering geometry. If we analyze the momentum conservation within the bulk material for backscattering situation, as in a typical Raman imaging experiment, we get the situation displayed in Fig. 1(a). Here, the momenta of the incident k_i and scattered k_s and the phonon q_a are all collinear. The situation changes, if scattering at a DW is concerned. Figure 1(b) shows the situation for z-cut incident scattering at a 180° domain wall, which is a typical geometry for the investigation of periodically poled LN. Here, the additional defect momentum q_{DW} will result in phonons with momentum q_b to participate in the scattering process, which are propagating at an oblique angle α with respect to the crystals optical axis. As Yang *et al.* experimentally demonstrated [33] in their analysis of the directional dispersion of $LiTaO_3$ and $LiNbO_3$, Raman spectra (intensity and peak positions) change heavily, when measured at different angles. The effect is, in particular large, when changing from z incident, which allows for observation of strong A_1-LO peaks, to x or y incident direction, which allows for the observation of the respective lower frequency, but high intensity A_1-TO phonons. This observation directly presents an explanation as to why A_1-LO phonons decrease in intensity at domain walls. Stone and Dierolf related specific spectral ranges of DW spectra to changes observed by Yang *et al.* in angular-resolved spectra [33]. The apparent major advantage of this explanation for the contrast mechanism is that the microscopic substructure of the domain wall is of no concern for the model and predictions are possible based on measurements of directional dispersions.

In summary, both models provide an explanation for the origin of the contrast observed at domain walls. Fontana *et al.* relate the spectral changes to the *microscopic* structure of the DW, i.e., strain or electric fields, while Stone and Dierolf consider the contrast at the DW as a *macroscopic* effect relaxing the selection rules. The goal of this work is to provide a comprehensive analysis about Raman spectra of 180° ferroelectric domain walls. Hereby, we analyze and interpret the obtained spectra with respect to both presented models. We have performed systematic measurements on domain walls for all scattering configurations on z- and y-cut samples in the common nonlinear materials $LiNbO_3$, $LiTaO_3$, and potassium titanyl phosphate ($KTiOPO_4$, KTP). While most previous works have only studied domain grids in z-cut geometries [1–15], we have specifically investigated domains on y-cut surfaces with Raman spectroscopy. This provides access to completely different phonon spectra. This enables us to develop a comprehensive view of the contrast mechanism. To evaluate the model of Stone and Dierolf, we have measured angular-resolved spectra also for all three materials and all scattering geometries. To address the microscopic model of Fontana *et al.*, we propose a simple atomistic model based on density functional theory (DFT) calculations, which enables a qualitative explanation of spectral changes from first principles.

This paper is structured in five main parts. Section II reviews the experimental details of our investigations, the angular-resolved measurements, and gives examples on the method of domain-wall imaging in LN, LT, and KTP. In Sec. III we evaluate the model by Stone and Dierolf on z-cut $LiNbO_3$, $LiTaO_3$, and $KTiOPO_4$ with respect to measured angular-resolved spectra. In Sec. IV, we expand our analysis to ferroelectric domain walls on y cut and evaluated the validity of this model in this geometry. In Sec. V we discuss a simple atomistic model for the DW contrast in y cut, which can not be explained based on the model of Stone and Dierolf. Before giving a conclusion in Sec. VIII, we will briefly discuss the limits of the presented models and point out open questions in Sec. VII.

II. METHODOLOGY

A. Experimental setup

The measurements in this work are performed with a custom built confocal Raman setup shown in Fig. 2. For excitation we use a frequency-doubled Nd:YAG laser at 532 nm in continuous wave operation with an output power up to 50 mW. The excitation beam is focused onto the sample via a infinity corrected objective lens (Mitutoyo Plan Apo 100×; NA = 0.7), which also collects the scattered light (backscattering

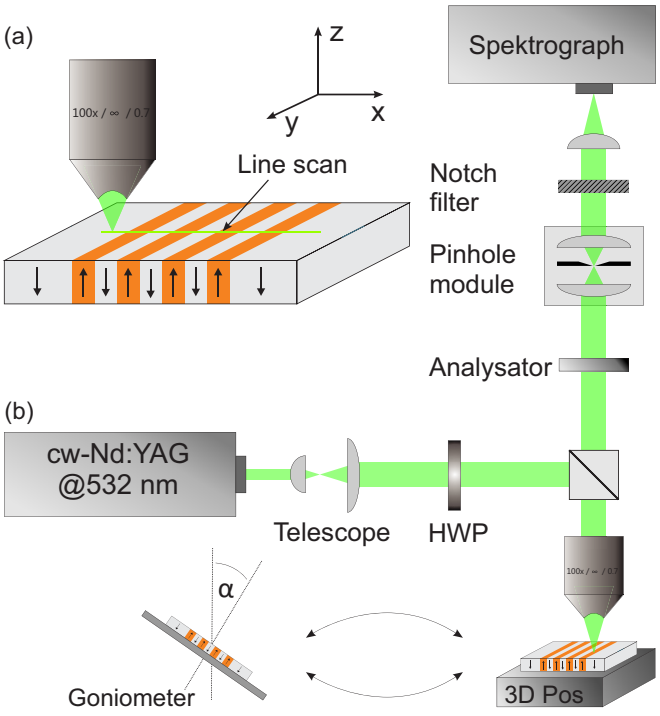

FIG. 2. (a) Sketch of the sample geometry. Here, a typical line scan is highlighted. (b) Sketch of the Raman setup used for analysis. For scanning, the samples are mounted to a piezodriven 3D positioner, which allows scanning with respect to a fixed focus. To measure the directional dispersion the 3D positioner is exchanged for a stepper motor with an attached sample mount.

operation). For depth discrimination, a confocal pinhole with a diameter of 10 μm is inserted in the detection path. Based on the parameters of the pinhole and objective lens, this results in a spatial resolution of <500 nm in lateral and <2000 nm in axial direction in vacuum, which decreases, when focusing into a highly refracting material especially along the axial direction [34]. However, this is of no concern for this study as investigations will be performed parallel to the DW planes. The spectral analysis is provided via a single-stage spectrometer with holographic grating and integrated notch filter (KOSI Holospec f/1.8i) with an attached CCD camera (Andor Newton, BI). For Raman imaging, a scanning procedure is necessary. In our setup, scanning is performed with respect to a fixed focus position. The samples are mounted on a piezostage (Piezosystem Jena Tritor), which offers a 2-nm resolution. To measure angular-resolved spectra, the three-dimensional (3D) positioner is substituted for a stepper motor with an attached sample mounting. The excitation and detection polarizations can be controlled via a half-wave plate (HWP) and analyzer, respectively.

In this paper polarization-dependent Raman spectroscopy will be performed. To unambiguously identify the scattering geometries the Porto notation $[k_i(e_i, e_s)k_s]$ will be used, where the vectors $k_{i,s}$ denote the direction of the incident and scattered light in crystal coordinates, while $e_{i,s}$ references the polarization of the light with respect to the crystal axis system [8,23,35].

TABLE I. Observable phonon mode branches and Raman tensor elements for backscattering configurations. For more details on the selection rules in these materials, the respective specialized papers should be referred [23,36–38].

	$LiTaO_3$ and $LiNbO_3$		$KTiOPO_4$	
Scattering geometry	Tensor elements	Phonon branch	Tensor elements	Phonon branch
$x(y, y)\bar{x}$	$a^2 + c^2$	A_1-TO + E-TO	b^2	A_1-TO
$x(y, z)\bar{x}$	d^2	E-TO	f^2	B_2-TO
$x(z, z)\bar{x}$	b^2	A_1-TO	c^2	A_1-TO
$y(x, x)\bar{y}$	$a^2 + c^2$	A_1-TO + E-LO	a^2	A_1-TO
$y(x, z)\bar{y}$	d^2	E-TO	e^2	B_1-TO
$y(z, z)\bar{y}$	b^2	A_1-TO	c^2	A_1-TO
$z(x, x)\bar{z}$	$a^2 + c^2$	A_1-LO + E-TO	a^2	A_1-LO
$z(x, y)\bar{z}$	c^2	E-TO	d^2	A_2-TO
$z(y, y)\bar{z}$	$a^2 + c^2$	A_1-LO + E-TO	b^2	A_1-LO

Taking the three main crystal axes into account, this means that nine different scattering geometries in backscattering, where $k_i = -k_s$, are possible. Depending on the scattering configuration different symmetry species of phonon modes belonging to different tensor elements will be detected. For the three analyzed materials, the resulting selection rules are listed in Table I. For more details on the selection rules in these materials, the respective specialized papers should be referred [23,36–38].

B. Angular-resolved Raman spectroscopy

The contrast for domain walls in Raman microscopy is explained by Stone and Dierolf by a relaxation of the selection rules by treating the domain wall as a large, planar defect. Therefore, it is expected that phonons propagating at oblique angles with respect to the wall will also participate in the scattering. In polar crystals, like LN, LT, or KTP, the phonon spectrum will change as a function of the propagation angle of the phonons, which is called directional dispersion. In the theory of directional dispersion [33,39–43] two types of phonons are distinguished. The first type are ordinary phonons, which do not shift and vary in spectroscopy under various angles, and extraordinary phonons, which shift under angular observation. This is a prominent effect in polar materials, such as ferroelectrics. This effect can be understood as the coupling of phonons to long-range electric fields. The terms "ordinary" and "extraordinary" are chosen in analogy to the ordinary and extraordinary optical axes. In particular, phonons propagating parallel to the extraordinary axis, the axis of the internal field, are subject to changes. In contrast to this, phonons in the ordinary plane are usually not subject to change. It should be noted that KTP is a biaxial material with three refractive indices. Hence, extraordinary phonons with a pronounced directional dispersion are also expected in the xy plane.

To measure directional dispersions, the samples are mounted on the goniometer stage and the sample was tilted with respect to the fixed focus axis. It should be noted that the outer tilt angle β does not represent the angle α at which the phonon is excited. Due to refraction the excitation angle is

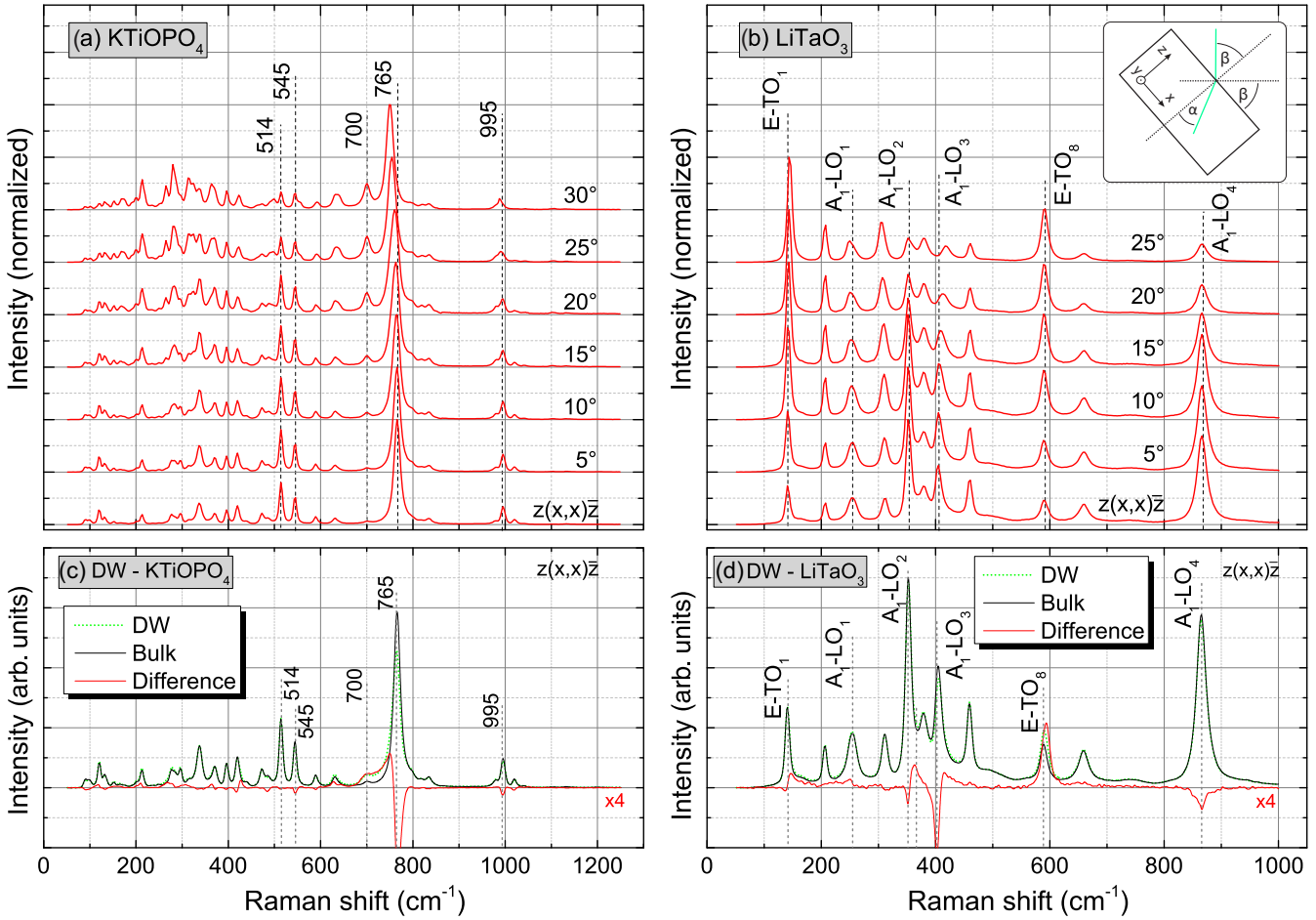

FIG. 3. (a), (b) Show the angular-dependent Raman spectra of KTP and LT. The crystal is tilted in steps of 5° along the y axis as shown in the inset. The light polarization is kept fixed according to the 0° scattering geometry $z(x, x)\bar{z}$. Spectra of DWs for KTP and LN have been measured [(c) and (d)]. Several modes, which show a pronounced angular-dependent behavior [(a) and (b)], also show a sensitivity for domain walls [(c) and (d)].

changed according to the inset in Fig. 3. The angles have been corrected by using Snell's law

$$n_{\text{air}} \sin(\beta) = n_{\text{material}} \sin(\alpha). \tag{2}$$

Lithium niobate has an extraordinary refractive index at 532 nm of approximately $n = 2.23$. This means that the sample needs to be tilted by 47° to record the spectrum at $\alpha = 20°$. Alike, the corrections have been performed for KTP and LT.

Figures 3(a) and 3(b) show a series of Raman spectra taken every 5° of tilting. Due to internal reflection only spectra up to approximately 25° in LN and LT and 30° in KTP could be taken. The light polarization in the experimental setup was kept fixed according to the starting scattering geometry, which in this case was $z(x, x)\bar{z}$ in Porto notation. The spectra are normalized to maximum after the dark counts has been subtracted. For better visibility, they are separated by 0.5. This enables to compare the relative changes in the directional-dependent spectra with the features of the DW spectrum. For an easier comparison, some spectral features have been highlighted. The modes in $LiNbO_3$ and $LiTaO_3$ are labeled with respect to the commonly accepted assignments [23,35,38,44]. For $KTiOPO_4$, no generally accepted assignment is available, therefore, the approximate mode wave numbers are given.

C. Raman imaging and samples

Three samples have been analyzed. The periodically poled lithium niobate and lithium tantalate samples have been commercially obtained from Deltronic Crystals, Inc. The lithium niobate crystal features a period length of $\Lambda = 28.3$ μm and a duty cycle of 60:40, while the lithium tantalate crystal is poled with a period length of $\Lambda = 28.9$ μm with a duty cycle of 50:50. Both samples are fabricated from congruent material. To enable the optical analysis, both samples have been polished on one z face and one y face, respectively. Here, the polishing step also makes sure that any etching pattern is removed.

The KTP sample was fabricated in the in-house technology [8,45] in Paderborn. At first, a commercial flux grown KTP wafer is cut into pieces with dimensions of about 10 (x) by 6 (y) by 1 (z) mm^3. The samples are immersed in a pure KNO_3 melt to homogenize the potassium stoichiometry. In a photolithographic patterning step, a periodic photo resist structure is fabricated on the z face of the crystals. Both sides

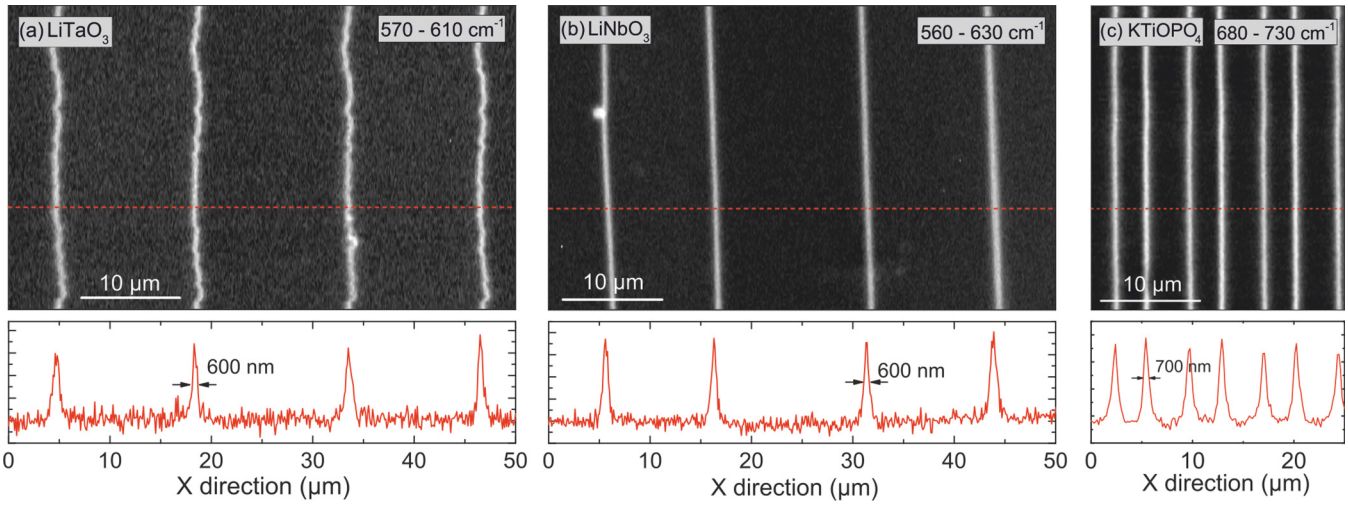

FIG. 4. Raman imaging is demonstrated for $LiNbO_3$, $LiTaO_3$, and $KTiOPO_4$ samples. Each image is created using the integrated intensity in a specified spectral range of the Raman spectrum, which was chosen based on previous works [2,4,8,10,14]. The graph below each image gives a cross section along the red dashed line. Here, domain-wall signatures down to 600 nm can be observed, which is limited by optical resolution, while the domain transition may be much smaller. The Raman spectra were taken in $z(x, x)\bar{z}$ scattering geometry.

are electrically contacted and several high voltage pulses are applied to the sample to periodically pole the crystal. The poling progress is monitored with an *in situ* optical monitoring based on the electro-optic effect [46]. The domain structure features a poling period of $\Lambda = 7.6$ μm and a duty cycle of approximately 50:50. Alike, the KTP sample has been polished on the z face and one y face for optical analysis. All samples have domain walls oriented parallel to the the y axis according to Fig. 2.

Figure 4 shows ferroelectric domain structures revealed by Raman imaging on all three samples. The images on the $LiNbO_3$ and $LiTaO_3$ samples show a 50×30 μm^2 $(x \times y)$ surface with visible DWs, while the $KTiOPO_4$ shows a smaller region of 25×30 μm^2 $(x \times y)$. For the scans, the focus was placed typically 5 to 10 μm below the sample surface, to ensure that no surface phonon spectrum will interfere with the measurements [47]. For each material spectral ranges are known, which show a systematic decrease or increase in intensity. A straightforward and convenient method to generate images of domain wall is to integrate the intensity in such a spectral range [10]. This integrated intensity is then plotted with respect to the spatial coordinates of the measured spectrum to reveal the domain structure. For our images, we chose material-specific spectral ranges, which are known to provide an increased signal at DWs. In detail, we chose the range from 570 to 610 cm^{-1} for LT [10], the region from 560–630 cm^{-1} in LN [2,4,14], and the region of 560–630 cm^{-1} for KTP [8].

The results are shown in Figs. 4(a)–4(c). Here, the period length differences as well as the different duty cycles can be seen. Below each image a plot of the intensity profiles along the red dashed line is given. In this experiment, we detect DW signatures [full width at half-maxima (FWHM)] down to 600 nm. This is mainly moderated by the resolution limit of optical microscopy and not by the size of the domain wall, which is likely to be significantly smaller than this. Here, other methods, e.g., PFM, reveal domain transitions down to be 20–80 nm for LN or KTP [48] or even less [17–19]. The observed signatures are well comparable to typical Raman signatures of DWs [1–15] and therefore are typical candidates for the analysis of the contrast mechanism.

III. DW SPECTRA IN z INCIDENT

Based on the imaging procedure discussed in the previous section individual domain walls are located and Raman spectra are measured. In Figs. 3(c) and 3(d), two examples for a DW spectrum for $KTiOPO_4$ and $LiTaO_3$ are shown. Here, the DW spectrum is given in dashed green lines. For comparison, a bulk reference spectrum is also shown. Both spectra are shown as measured and are not normalized. The comparison reveals shifts and intensity variations in several modes, but no additional lines. This observation is consistent with literature [6,8]. To better highlight the differences, it is convenient to plot the difference spectrum. Here, the bulk spectrum is subtracted from the DW spectrum $[I(\mathrm{DW}) - I(\mathrm{bulk})]$ and plotted below in red. The macroscopic model by Stone and Dierolf associates the spectra of oblique propagating phonons with the DW spectrum. Indeed, in a direct comparison many features of the domain-wall spectrum can be connected to angular-dependent changes [Figs. 3(a) and 3(b)].

For a systematic analysis, DW spectra and bulk spectra have been taken in all three independent scattering configurations $[z(x, x)\bar{z}$, $z(x, y)\bar{z}$, and $z(y, y)\bar{z}]$. The difference spectra have been calculated and plotted in the top panels in Figs. 5(a)–5(i). For reference the bulk spectrum in the respective geometry was added. The plots reveal DW related changes in all scattering configurations. In LN and LT, the $z(x, x)\bar{z}$ and $z(y, y)\bar{z}$ DW spectra are similar changes. This can be understood because both spectra will address the same Raman tensor element [23,35], as well as due to geometric reasons similar angular-dependent changes are expected. For KTP the situation is slightly different because the $z(x, x)\bar{z}$ and $z(y, y)\bar{z}$ spectra will show the same branch of A_1 phonons, but related to a different tensor element (compare Table I).

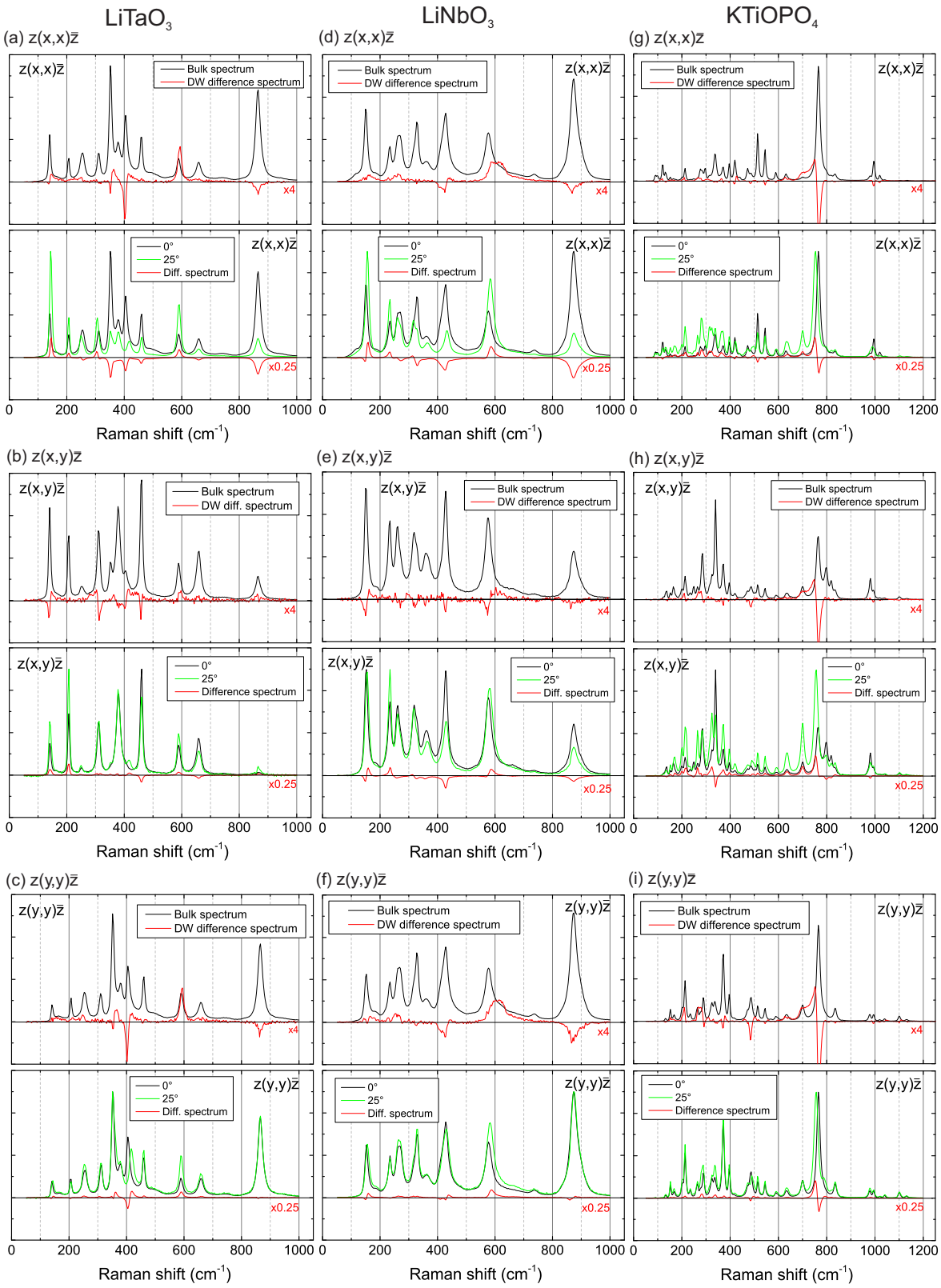

FIG. 5. The figure shows the spectral signatures of domain walls on z incident for all three materials in the top panels. Here, in black a bulk spectrum is given for reference, while the red line denotes the difference spectrum calculated from the measured DW spectrum $[I(\mathrm{DW}) - I(\mathrm{bulk})]$. Below are the 0° and 25° angular-resolved spectra, where 0° is equal to the bulk spectrum in the top panel. To highlight differences, also a difference spectrum is given $[I(25^\circ) - I(0^\circ)]$.

Nevertheless, the DW spectrum for both geometries shows similar changes, in particular, the red-shift and decrease of the most intense line at 765 cm^{-1}.

The goal is now to systematically compare domain-wall spectra and angular-resolved spectra in z incident. Figures 3(a) and 3(b) demonstrate that the spectral changes with respects to angle are continuous, which is consistent with literature [33]. Therefore, to identify the largest changes caused by angular dispersion it may be enough to compare two spectra, a 0° (bulk) spectrum and a 25° spectrum, which is the largest angle, which can be measured for all samples. Due to increased reflection at higher angles and changing scattering efficiencies, the spectra have been normalized similar to Figs. 3(a) and 3(b). These 0° (black) and 25° (green) spectra are plotted in the bottom panels in Figs. 5(a)–5(i). For a convenient comparison, a difference spectrum (red) between the 0° (black) and 25° (green) has been calculated similar to the method for the DW difference spectrum $[I(25°) - I(0°)]$.

Although this difference spectrum is calculated from normalized spectra, the accordances between the DW difference spectra and angular-resolved difference spectra are surprisingly large. Many of the observed features of the DW spectrum can be readily explained in this comparison. For example, in previous works it was observed that so-called A_1-LO [6,8,35] usually show a decrease in intensity at DWs. While other spectral ranges, where in x- or y-incident geometries extremely intense phonons are observed, e.g., A_1-TO, an increase of intensity is seen in the DW spectrum as well. Both of these observations can be readily understood based on the theory of directional dispersion. Pure A_1-LO phonons in polar crystals can only be observed in scattering configurations along the axis of the spontaneous polarization, which is the z direction. These phonons will gradually shift and disappear by tilting to any other crystal direction [33,39–43]. In contrast to this, pure so-called A_1-TO phonons can only be observed in geometries orthogonal to the z axis, i.e., the extraordinary plane. Therefore, these spectral ranges will increase in intensity at the DW. This, for example, explains the strong increase in LN at 620 cm^{-1} and at 580 cm^{-1} in LT, which is consistent with previous suggestions [6,23].

For the $z(x, y)\bar{z}$ geometries in LN and LT the predictions $[z(x, y)\bar{z}]$ are less conclusive. This is, however, expected as these geometries show so-called E-TO modes (see Table I). The E modes for LN and LT have no pronounced directional shifts, as the E-TO modes are ordinary modes and appear at the same frequencies after the respective full turn. Nevertheless, some contrast for the DW can be seen. This may be, at least partially, by the fact that the scattering efficiency will change as a different Raman tensor element will be addressed [35,44]. However, as we will see below, other effects may be present.

So far, we have shown that the model by Stone and Dierolf can sufficiently enough explain the changes observed at domain walls in z-incident geometry. Further, we have demonstrated that the analysis of angular-resolved spectra allows to predict the contrast behavior. The next question is if this model also provides reliable predictions for y-cut scattering configuration.

IV. DW SPECTRA IN y INCIDENT

To analyze DW spectra at y-incident geometry, locations of domain walls need to be identified. Most Raman investigations were performed in z incident though [1–16]. Therefore, domain-structure-sensitive phonons have to be identified first. To be able to also detect any subtle changes in the spectrum, we have fitted selected lines with a Lorentzian function of the form

$$I(\omega) = \frac{A}{2\pi} \frac{\delta}{(\omega^2 - \omega_c^2) + \delta^2/4}, \tag{3}$$

where the prefactor A gives the integrated intensity of the line, ω_c is the resonance or peak frequency, and δ specifies the FWHM of the line. This allows to investigate the changes of line shifts, intensities, and FWHMs. Figure 6 shows the result of such an investigation of a line scan of 100 μm on $LiNbO_3$. While the intensity A only shows a weak connection to the

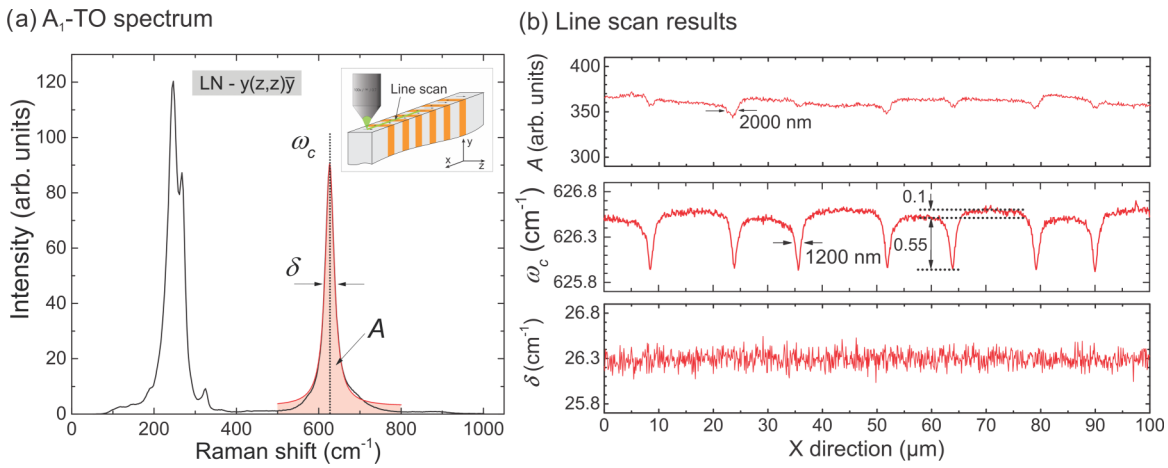

FIG. 6. (a) Raman spectrum taken in $y(z, z)\bar{y}$ scattering geometry for $LiNbO_3$. The A-TO_4 line has been fitted with a Lorentzian function. The inset demonstrates the measurement geometry, in which y-cut domains have been investigated. (b) Fitting results of a line scan on the $LiNbO_3$. The domain walls are associated with a clear shift of the peak frequency, while in the intensity only a light imprint can be seen.

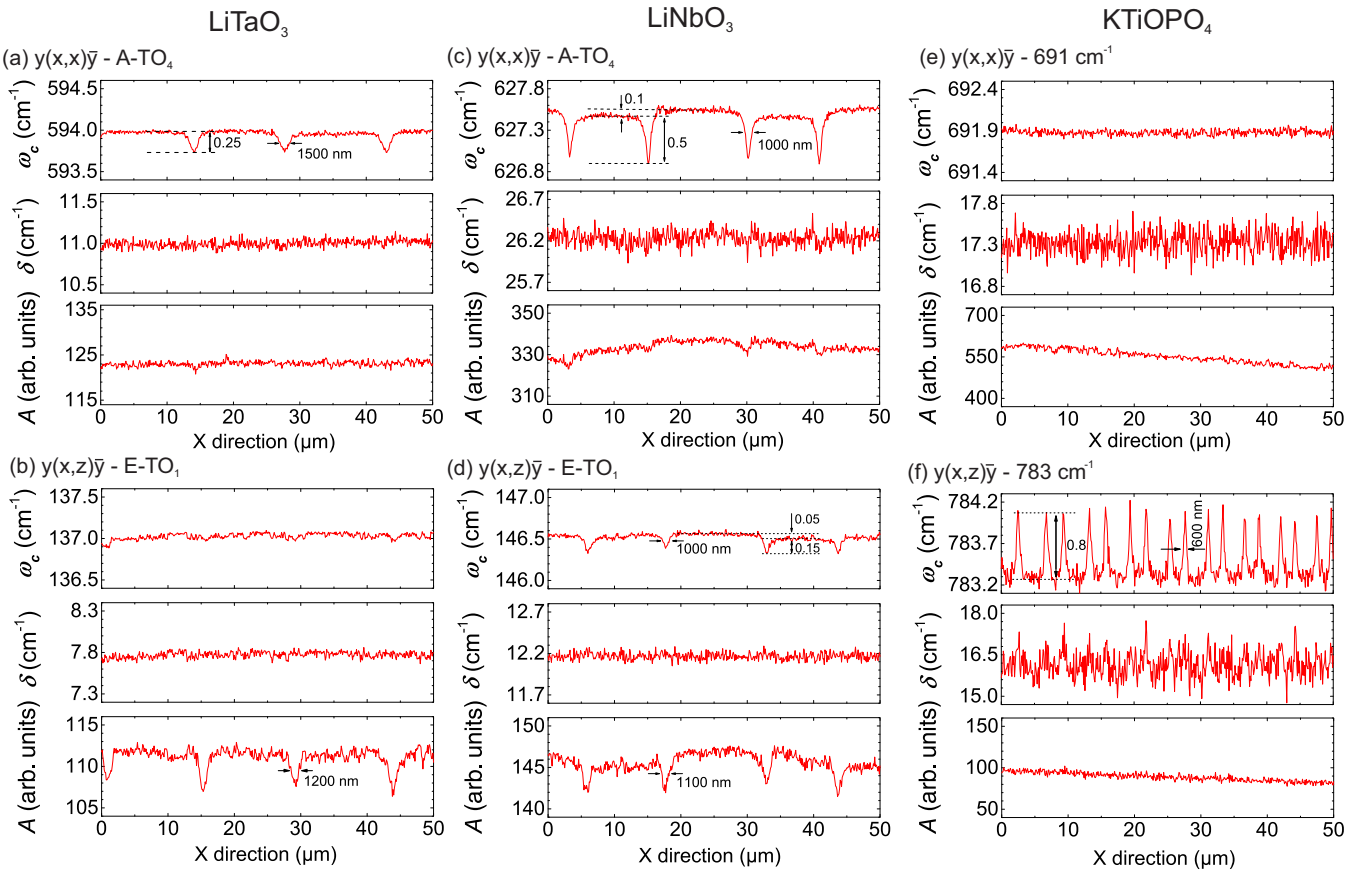

FIG. 7. The figure shows examples of results of lines scans for all three materials. Here, each phonon gives rise to a specific signature related to the presence of domain wall. While the DW signatures in $LiTaO_3$ and $LiNbO_3$ appear wider in y cut than in z cut, the DW signatures of KTP are of the same order. Here, however, only a contrast for $y(x, z)\bar{y}$ is observed. The modes in LN and LT have been assigned according to the usual naming conventions [23,35,38].

domain walls, a shift in the peak frequency ω_c can be seen, which is related to the DWs. The period length of 28.3 μm and the 40:60 duty cycle are reproduced very well, which demonstrates that domain wall imaging on y cut is possible.

For each sample, such line scans have been performed in different scattering configurations and several modes have been investigated for connections to the domain walls. Here, Fig. 7 shows an example for one mode on each sample in $y(x, x)\bar{y}$ and $y(x, z)\bar{y}$ polarizations.

From the viewpoint of the macroscopic model y-cut incident domain-wall imaging comes with a substantial difference. Figure 1(c) shows that scattering at the DW may excite mixed phonons propagating in the xy plane (or ordinary plane) of the crystal. Here, many phonons branches will exhibit no directional dispersion [39], as also demonstrated in experiments [33,40]. This can also be seen from the selection rules summarized in Table I, where for x and y incident in most geometries the same phonon branches belonging to the same tensor elements will be addressed. Therefore, no directional dispersion is expected for most phonons is expected.

The bottom panels in Figs. 8(a)–8(i) show the results of the angular-resolved measurements for y-incident geometries, which were prepared as described above. Indeed, we see only small changes between the 0° and 25° spectra. For LN and LT the only exception is the $y(x, x)\bar{y}$ geometry. Here, according to the selection rules (Table I) the so-called E-LO phonons can only be observed in this geometry. Therefore, this phonon may change at the DW. In the LT spectrum this can be seen, for example, for the line at ≈460 cm^{-1}, which changes with respect to the angle. For the other two geometries, however, no changes are expected and observed with respect to angle. The situation for $KTiOPO_4$ is different, because it is a biaxial crystal with an additional polar axis. This also means that long-range fields and extraordinary phonons, i.e., phonons with a directional dependence in the xy plane, do exist. Comparing the selection rules in Table I, one can see that the $y(z, z)\bar{y}$ and $y(x, x)\bar{y}$ exhibit no directional dispersion because in the $x(z, z)\bar{x}$ and $y(x, x)\bar{y}$ geometries also A_1-TO phonons will be seen. Here, only for $y(x, x)\bar{y}$ a slight contrast may be expected, as the phonon spectrum in $x(y, y)\bar{x}$ is belonging to a different Raman tensor element. However, the spectral differences are relatively small [8]. The only geometry, where a strong DW contrast in KTP is expected, is $y(x, z)\bar{y}$ because here a transition from B_1 $[y(x, z)\bar{y}]$ to B_2 $[x(y, z]\bar{x})$ phonons is expected. Indeed, this is also what is observed in the experiment.

Similar to the previous section, domain-wall spectra on y incident have been systematically measured for all geometries. These are plotted in the top panels in Figs. 8(a)–8(i). While for KTP in agreement with the prediction, only a significant domain-wall contrast is observed for $y(x, z)\bar{y}$ [Fig. 8(h)], for LN and LT a domain-wall contrast for all

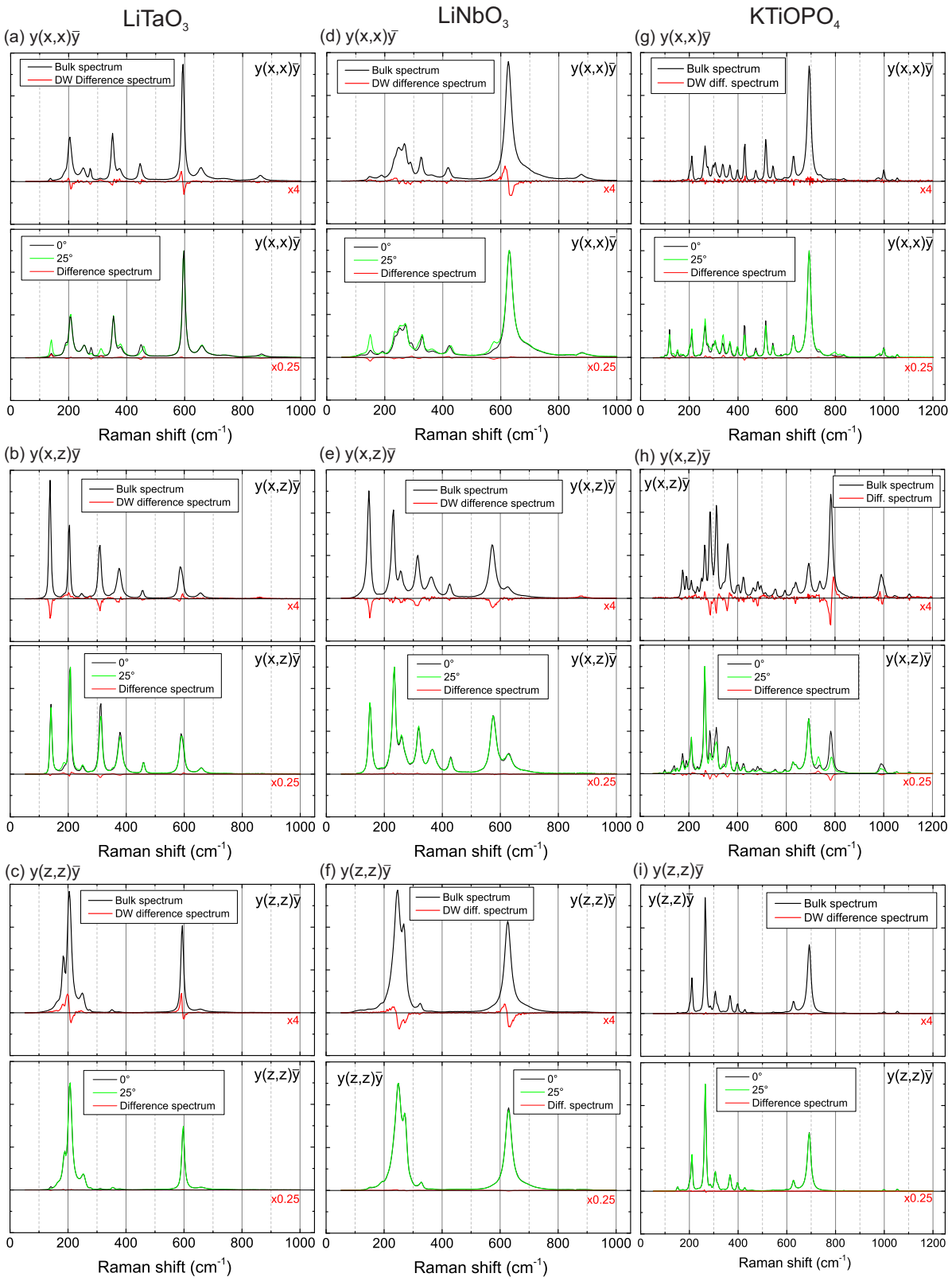

FIG. 8. The figure shows the spectral signatures of domain walls on y cut for all three materials in the top spectra. Here, in black a bulk spectrum is given for reference, while the red line denotes the difference spectrum calculated from the measured DW spectrum [I(DW) − I(bulk)]. Below are the 0° and 25° angular-resolved spectra, where 0° is the spectrum in the given scattering geometry. Here, to highlight differences, also a difference spectrum is given [$I(25°) - I(0°)$].

geometries is seen. For example, the most dominant peak in the $y(x,z)\overline{y}$ geometry for LT [Fig. 8(h)] at about 590 cm^{-1} shows a large shift towards lower frequencies. This is in strong contrast to the observation from the directional dispersion. The predictions based on the directional dispersion reproduce the changes of the E-LO modes well, which is, for example, seen in the behavior of the ≈460 cm^{-1} line. Even more striking are the differences for the $y(z,z)\overline{y}$ spectra for LT and LN, where no contrast at all was expected, and yet intensity changes and shifts are observed [Figs. 8(c) and 8(f)], which also lead to high-contrast images as shown in Figs. 7 and 6.

It appears that the macroscopic model based on the directional dispersions can only explain the DW contrast in KTP and the behavior of the E-LO in LN and LT [$y(x,x)\overline{y}$], while the major changes in the LN and LT spectra remain not explained. To explain this behavior, we take a look at the line scans of DWs presented in Fig. 7.

While the signatures of the domain walls for $KTiOPO_4$ show a similar width of 600 nm in y cut as in z cut, we observe for $LiNbO_3$ and $LiTaO_3$ signatures with half-widths between 1000 and 2000 nm in Figs. 8 and 6. This is significantly larger than the results observed in z cut in the Sec. II (Fig. 4). It should be stressed again at this point that the results for z cut and y cut both have been obtained on the same samples and with the same experimental setup. The only difference is the scattering geometry. This suggests that we have a different, physical mechanism (with longer influence range) being responsible for the spectral changes than the macroscopic relaxation of selection rules. And this mechanism is, at least in this experiment, only present in $LiNbO_3$ and $LiTaO_3$, but not in $KTiOPO_4$. The explanation may be the aforementioned strain and/or electric fields in agreement with the suggestion of Fontana *et al.* [4].

Indeed, in particular in congruent $LiNbO_3$ and $LiTaO_3$ a multitude of effects have been observed in the vicinity of domain walls. Strain fields in the order of 10 μm have been observed by x-ray topography spanning around domain walls [28,29]. As $LiNbO_3$ and $LiTaO_3$ are piezoelectric, this strain will likely be associated with an electric field. Indeed, electric fields are present in the region of domain walls in congruent lithium niobate, as demonstrated by Dierolf *et al.* with luminescence microscopy [7,49]. Here, they detected fields between 4 and 6 kV/mm in a 4 to 10 μm range around the domain wall. These strains and electric fields are on the same length scale as changes in birefringence and refractive index, which have been observed in scales from 3 to 20 μm around domain walls in LN and LT [7,50,51]. In this context, Gopalan *et al.* pointed out different response length scales for different analysis methods of domain walls, in agreement with our observation they detected DW signature width of 1.5 μm with Raman spectroscopy [7]. Why is no such behavior observed for $KTiOPO_4$ in our experiment? Here, the reason may lie in the specific material properties of $KTiOPO_4$, which is known for its very high ionic conductivity [52]. If any strains or electric fields are present in $KTiOPO_4$, they will be soon masked by a charge rearrangement. This may also be the reason why domain-wall signatures are often reported to be smaller in KTP compared to LN or LT [48].

The presence of electric fields and their influence on the Raman spectrum in lithium niobate allows to understand another observation in the y-scan domain walls. In the line scans of lithium niobate in Figs. 7(c), 7(d), and 6 one can see in the peak frequencies of the respective modes, do not only show a contrast for the domain wall, but apparently also a different level between domains of a different polarity. Here, for the A_1-TO phonon a difference of $\Delta\omega_c = 0.1$ cm^{-1} is seen, while for the E-TO_1 phonon a shift of $\Delta\omega_c = 0.05$ cm^{-1} is detected. This can be explained based on the result of Stone *et al.*, who analyzed the z-cut Raman spectrum of stoichiometric and congruent lithium niobate under applied electric fields oriented parallel to the z axis before and after domain inversion [27]. They detected for all of their analyzed phonons a linear shift of the mode frequency with respect to the applied electric field, as well as a frequency difference between domains of different orientations. Depending on the phonon they detected differences $\Delta\omega_c$ between 0.24 and 0.64 cm^{-1} of the peak frequencies of phonon between domains of different polarity.

According to Stone *et al.,* the proportionality constants between frequency shift and electric field β_E have values between 0.01 to 0.03 cm^{-1}mm/kV for most modes. Unfortunately, they did not provide data for A_1-TO_4 from y cut because they measured from z cut, which only shows A_1-LO modes. However, a β_E between 0.01 to 0.03 cm^{-1}mm/kV will correspond to an internal field of 3–10 kV/mm based on the A_1-TO_4 of $\Delta\omega_c = 0.1$ cm^{-1}, which is a reasonable magnitude for the internal fields reported for congruent material [49,53–55]. Taking their proportionality constant for the E-TO_1 and assuming it can also be applied in y-cut spectra, we obtain an internal electric field of 2 kV/mm with $\beta_E = 0.024$ cm^{-1}mm/kV and $\Delta\omega_c = 0.05$ cm^{-1}. A different absolute field strength determined by different phonons may also suggest off-axis E-field or strain components, as the E-TO_1 has a displacement pattern mainly in the xy plane in contrast to the A_1-TO_4, which has has a total-symmetric displacement pattern conserving the symmetry along the z axis [23].

V. ATOMISTIC MODEL SIMULATIONS

The previous section suggests that microscopic changes, i.e., strain and electric fields, are responsible for the changes in the Raman spectrum for y-incident geometries in LN and LT. To assess the changes qualitatively, we study the effect of strain on the Raman spectra by means of a simplified atomistic model. Ideal ferroelectric domain walls are expected to be Ising type with the spontaneous polarization constantly decreasing towards the domain transition and a spontaneous polarization of $P_s = 0$ defining the DW transition. While many experimental and theoretical studies hint at non-Ising DW components in real materials [30,56], we only consider the dominating Ising type. Therefore, we consider the domain-wall region as a homogeneously strained bulk material. The strain direction is chosen along the reaction coordinate which transforms the ferroelectric (FE) into the paraelectric (PE) phase. Therefore, the model's key feature is a linear interpolation between the PE and FE phases of the rhombohedral unit cell of LN/LT (Fig. 9), i.e., lattice vectors as well as atomic coordinates are linearly interpolated between their respective

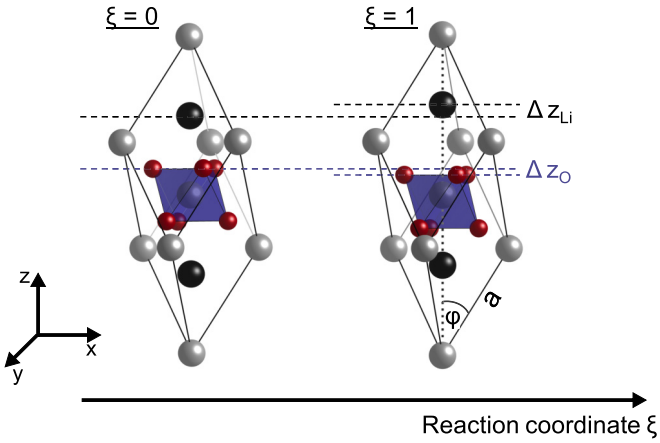

FIG. 9. Rhombohedral unit cell of LN/LT for different states along the reaction coordinate ξ between the ferroelectric ($\xi = 1$) and paraelectric phase ($\xi = 0$). O atoms are indicated in red, while white and black circles represent Nb/Ta and Li, respectively. Note the displacement Δ z_O between the oxygen octahedron and the central niobium along the ferroelectric z axis as well as the displacement Δ z_{Li} of the lithium sublattice. Rhombohedral lattice constants φ and a are indicated.

PE and FE values:

$$\vec{a}(\xi) = \xi \cdot \vec{a}_{\mathrm{FE}} + (1 - \xi) \cdot \vec{a}_{\mathrm{PE}} \tag{4}$$

with $0 \leqslant \xi \leqslant 1$. This interpolation accounts for the change of internal polarization assuming an ideal Ising-type along the z axis, as well as strain effects along/perpendicular to z. The vicinity of the domain wall is therefore approximately modeled by domains with varying reaction coordinates ξ along the paraelectric-ferroelectric reaction pathway, with the domain-wall center being approximated to be in a pure paraelectric ($\xi = 0$) and the bulk material to be in a pure ferroelectric phase ($\xi = 1$). Density functional theory ground-state calculations have then been performed within the generalized gradient approximation (GGA) as parametrized by Perdew, Burke, and Ernzerhof (PBE) [57,58] and implemented in the Vienna *ab initio* simulation package (VASP) [59,60]. The wave functions were expanded in plane waves up to a cutoff energy of 600 eV, while the integration over the Brillouin zone has been carried out using a $5 \times 5 \times 5$ k-point mesh. Atomic positions and lattice vectors were relaxed until the total force acting on the system fell below a threshold value of 0.01 eV/Å. The resulting rhombohedral lattice constants of LN/LT within the ferroelectric and paraelectric phases are compiled in Table II. Phonon eigenvectors and differential Raman scattering efficiencies have been calculated via finite-difference routines. For numerical details we refer to Ref. [35]. In that work it has been shown that our DFT approach well reproduces the measured bulk Raman data of LN and LT. Due to the neglect of long-range electric fields accompanying LO phonon modes, our theoretical phonon spectra are limited to TO phonons, which however is no strong limitation to reproduce effects in y-cut spectra, where only the weak E-LO modes are present.

Since the changes of strain and internal polarization in the vicinity of a domain wall are considered to be relatively small (in the order of 10^{-4}) [7], only values of $\xi = 1$ (pure ferroelectric state) and $\xi = 0.95$ are considered in this work. A lattice distortion of that size accounts for strain values of $\epsilon_{x,y} = 3.8 \times 10^{-4}$ and $\epsilon_z = -7 \times 10^{-4}$ in the case of LN and $\epsilon_{x,y} = 3.3 \times 10^{-4}$ and $\epsilon_z = -3.7 \times 10^{-4}$ for LT. The internal polarization additionally decreases by $\Delta P_{\mathrm{LN}} = 33.77\,\mathrm{mC/m^2}$ and $\Delta P_{\mathrm{LT}} = 25.73\,\mathrm{mC/m^2}$ with respect to the ferroelectric phase, which amounts to a decrease 4.75% and 5.15%, respectively.

TABLE II. Rhombohedral lattice parameters a (in Å) and ϕ (in degrees) of the relaxed LN and LT cells in their FE and PE phases. Experimental values refer to Refs. [61] for $LiNbO_3$ and [62] for $LiTaO_3$.

	LN		LT	
Phase	FE	PE	FE	PE
a^{PBE}	5.59	5.54	5.53	5.51
a^{expt}	5.50	5.54	5.47	5.49
ϕ^{PBE}	32.63	33.20	32.90	33.27
ϕ^{expt}	32.73	33.49	32.92	33.27

Raman spectra as well as difference spectra between the two geometries have been calculated for the y-cut geometry and plotted in the bottom panels in Fig. 10. The top panels show again the results of the y-cut measurements from the previous section. As a general trend, the model qualitatively reproduces the measured deviations from the bulk spectra by revealing a red-shift for almost all modes. The influence is very dominant on the A_1-TO modes [23,35,38] in the $y(x, x)\overline{y}$ and $y(z, z)\overline{y}$ scattering geometries. This can be explained by the large overlaps between the A_1-TO eigenvectors and the paraelectric-ferroelectric displacement vector (94% and 69% in case of the A_1-TO_1 mode of LN and LT, respectively) and is also seen in the soft-mode behavior of these modes [63–66]. In the $y(x, z)\overline{y}$ geometry E-TO modes are observable. In the experiment, we observe a decrease in intensity for all modes, while theory also suggests a shift. However, the theory suggests shifts of smaller magnitude for the E-TO modes compared to the A_1-TO modes, which may not be resolvable in experiment. The largest shift is predicted for the E-$TO_{5/6}$ double peak [23,35,38] at approximately 350 $\mathrm{cm^{-1}}$ for LT and 340 $\mathrm{cm^{-1}}$ for LN, which shows a blue-shift in contrast to all other modes. Indeed, this is also observed in the experiment for both materials.

In conclusion, it is seen that a simple model accounting for the structural changes in the vicinity of domain boundaries is able to qualitatively reproduce many experimentally observed features. Of course, a refinement of the model including different types or directions of strain is indicated, which may in the future allow for a deeper understanding of the domain-wall surroundings in $LiNbO_3$ and $LiTaO_3$.

VI. SIGNATURES OF STRAIN FOR z INCIDENT

If electric fields and strain fields are responsible for the contrast on y cut, then DW signatures related to strain may also be detected from z cut. The data in Sec. III indicated that the signatures in the $z(x, y)\overline{z}$ geometries for LN and LT

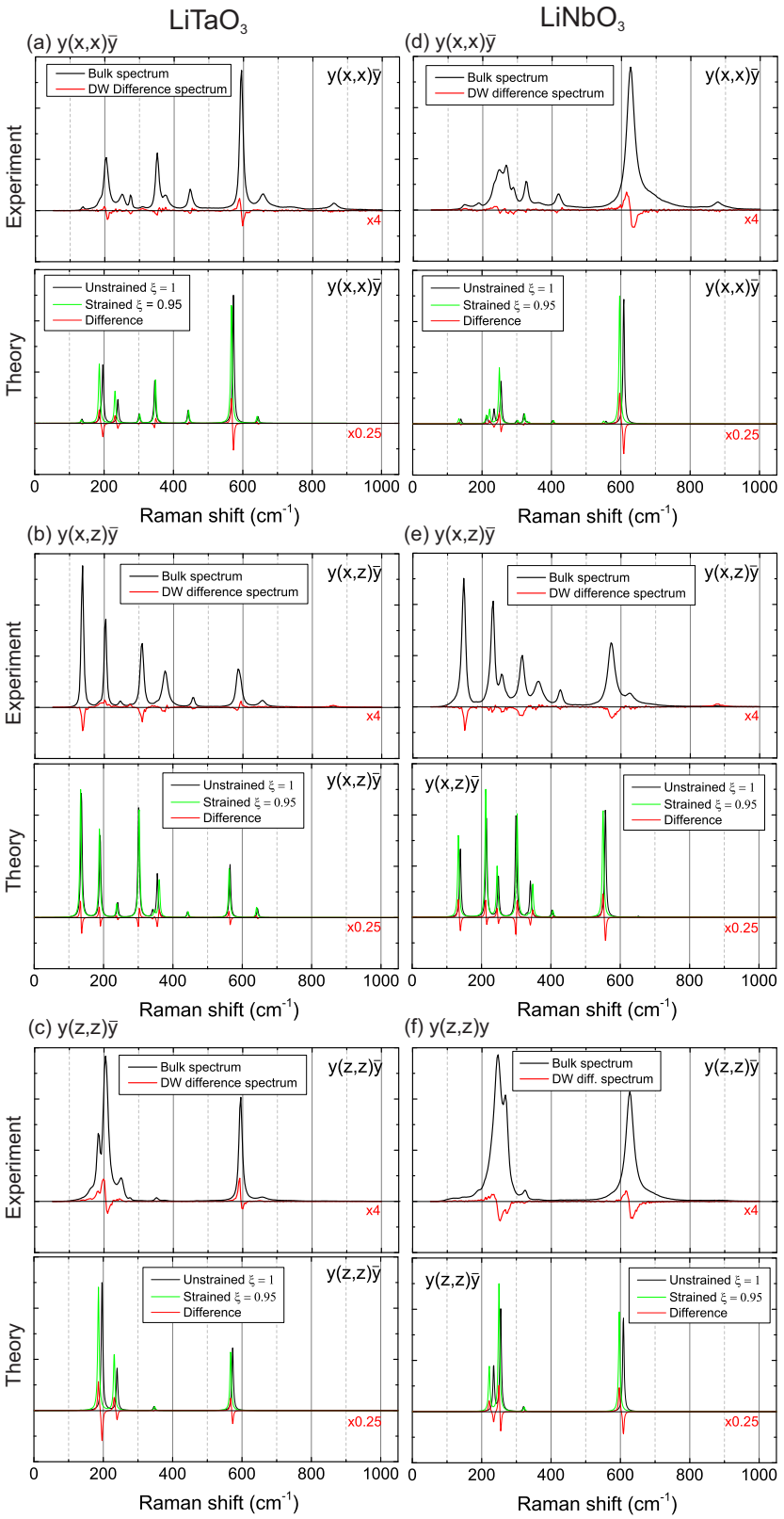

FIG. 10. The bottom panels show the theoretical Raman spectra of LN/LT in the y-cut polarization configurations. Spectra of both materials in their ferroelectric phase ("unstrained," $\xi = 1$) as well as in a distorted geometry corresponding to a displacement of 5% along the ferroelectric-paraelectric reaction pathway ("strained," $\xi = 0.95$) are depicted alongside their corresponding difference spectra. The top panels show the respective experimental results.

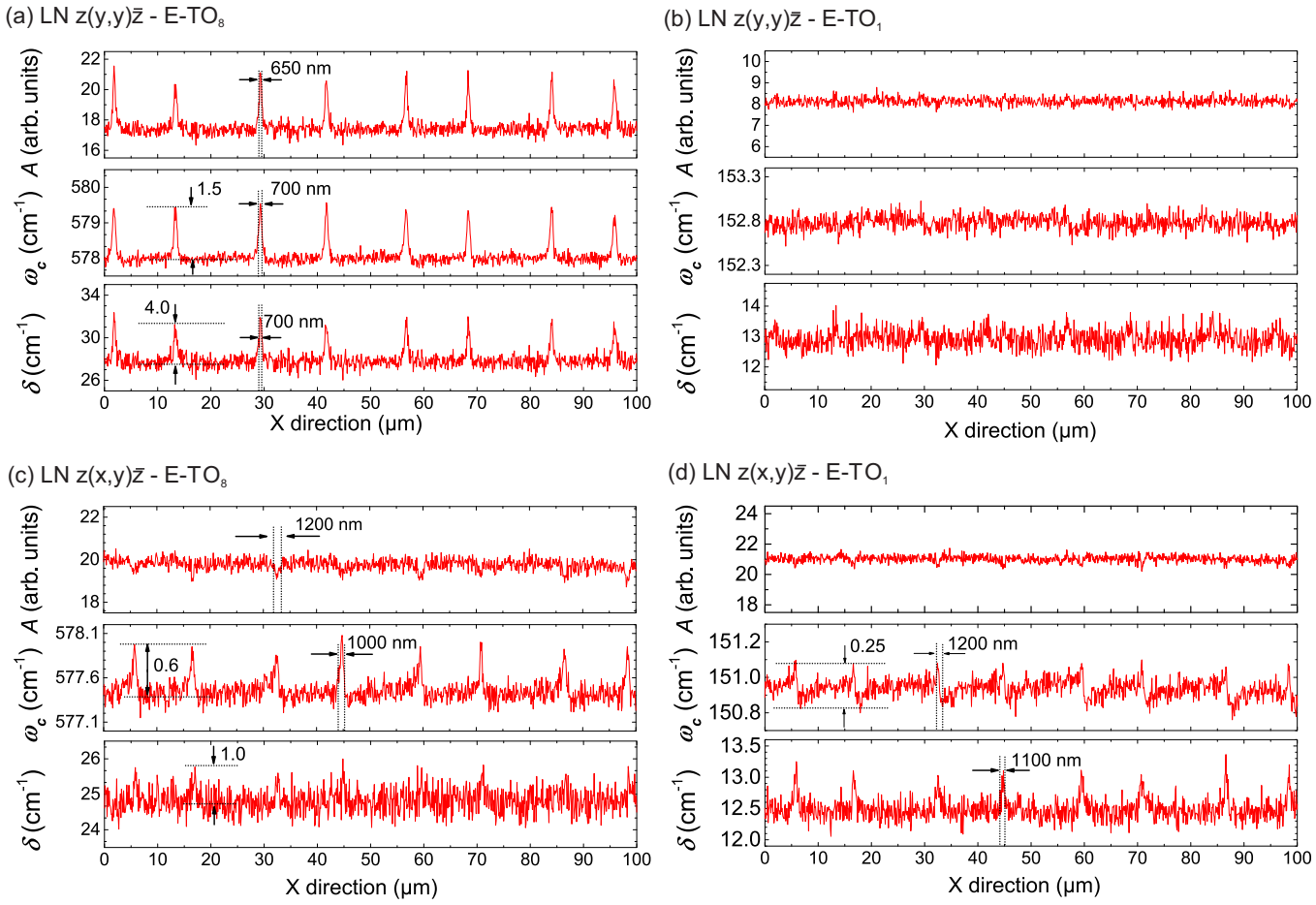

FIG. 11. We have investigated the peak frequency, integrated intensity, and FWHM for the E-TO_8 and TO_1 phonon from z cut in lithium niobate in $z(y, y)\bar{z}$ and $z(x, y)\bar{z}$.

cannot be understood in terms of directional dispersion. To analyze this behavior, two line scans comparing $z(y, y)\bar{z}$ and $z(x, y)\bar{z}$ geometries have been performed on LN. On both spectra we have selected the same phonons for an analysis of FWHM, peak frequency, and intensity as described at the beginning of Sec. IV. The results of these line scans are plotted in Fig. 11. Figure 11(a) shows the results for the so-called E-TO_8, where we detect an increase in all properties at a DW signature width of 600–700 nm. This DW signature can be readily explained in terms of the macroscopic model due to the optical resolution limited width and the behavior of the modes. According to our analysis, as well as previous investigations this mode shows a shift to higher frequency as part of its directional dispersion [33]. For the results on the E-TO_1 in the same geometry we only detect minor influences of the domain wall.

However, if we change the scattering geometry to $z(x, y)\bar{z}$ and analyze the same phonons again, we receive a different response with respect to the DW and larger signatures in the 1000 to 1200 nm range [Figs. 11(c) and 11(d)]. In agreement with the difference spectrum in Fig. 5(e), the E-TO_8 ($\approx$580 cm^{-1}) shows a decrease at the domain wall, while in the intensity an asymmetric shift to higher frequencies is observed. Here, the spatial width of the domain-wall signatures are larger (<1000 nm) than in $z(y, y)\bar{z}$, which again indicates that these shift can not be understood in terms of directional dispersion and lifted selection rules alone. An unusual behavior is seen for the results of the E-TO_1 ($\approx$151 cm^{-1}) in crossed polarization in Fig. 11(c). While the point spectrum in Fig. 5(e) suggested a slight shift to higher frequencies at the domain wall, we now see here that we actually see a sawtooth pattern, where the frequency apparently increases towards the domain wall and decrease within 1200 nm across the DW. This is definitely not explained by a change in selection rules, which should only be localized at the domain transition. According to the data of Stone *et al.* [27], the frequency drop of $\Delta\omega = 0.25$ cm^{-1} refers to a drop in electric field of approximately 10 kV/mm, which according to our data then rises again towards the next domain transition. It should be noted that Stone *et al.* only applied field along the z axis of the crystals. Here, the direction of the E field is currently unclear and it is possible that the E-TO phonons in $z(x, y)\bar{z}$ geometry may couple to off-optical-axis electric fields, which are also suggested in LN [67]. The range of the influence of the domain wall appears in this case to be in the order of $10-20\,\mu$m, which is in agreement with the observations by Dierolf *et al.* [49]. This shows that many things are left to understand in the substructure of the domain transition in lithium niobate and tantalate.

Our analysis suggests that the $z(x, y)\bar{z}$ DW spectra are explained not by the directional dispersion, but by strain. Therefore, the theoretical model from the previous section

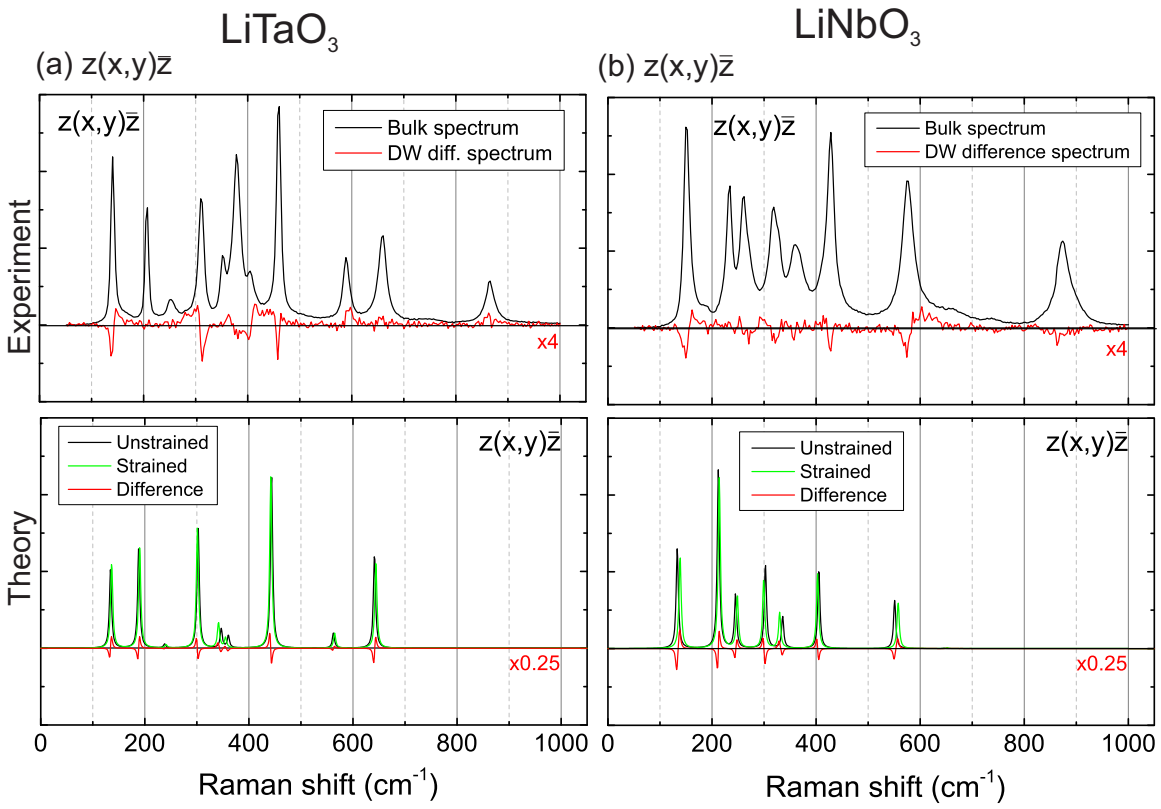

FIG. 12. The bottom panels show the theoretical Raman spectra of LN/LT in the $z(x, y)\bar{z}$ geometry. The top panels show the respective experimental results.

should be applicable. Figure 12 shows a comparison of the calculated and the measured spectra for $z(x, y)\bar{z}$ geometry. The theoretical results indeed predict most of the spectral changes.

VII. OPEN QUESTIONS

Although our work is able to explain the general behavior of the Raman contrast mechanism in poled bulk crystals, there are many peculiarities in these complex materials, which will influence the vibrational properties. Previous work has shown that point defects allocate at and in the vicinity of domain walls and domain walls do interact heavily with defects [7] and defects have an imprint in Raman spectra [22]. Our work on congruent LN and LT showed no qualitative differences in comparison to the previous work on stoichiometric material [6] with respect to the macroscopic model. This is not surprising because the substructure of the domain wall is of no concern. However, the DW contrast due to microscopic interaction, as we observed for the y-incident geometry in LN and LT, may completely vanish in stoichiometric material due to the reduction or absence of internal fields [53–55]. This will make stoichiometric LN and LT similar to KTP. In this context, the recent work by Nataf *et al.* demonstrates that MgO doping in LN, which lowers the intrinsic fields and the number of defects [68], also reduces the width of DW signatures in Raman spectroscopy with increased doping levels [16]. Similar annealing can lower the internal field and stresses [69], while annealing also homogenizes domain interfaces [70] and therefore alters the contrast behavior.

Many Raman investigations have observed a contrast between recently switched ("as-poled") and virgin ("as-grown") domains [5,14,16]. This contrast was explained in terms of residual surface charges, similar to our observations and the experiment by Stone *et al.* [27]. Related to this, different Raman spectra for $+z$ and $-z$ surfaces on lithium niobate have been predicted theoretically and observed in the experiment [47]. To exclude any surface effects, we measured well away from the surface. In the past, DWs of head-to-head, tail-to-tail, or arbitrary inclination have been observed with PFM and Cherenkov second-harmonic generation [71]. Any domains with an inclination with respect to the spontaneous polarization are charged [72], which may result in screening of space charges. Both surface effects and unusual domain orientation may influence the contrast mechanism, which is of particular importance when ridge structures [73,74] or the recent fabrication of domain grids in thin film LN [75,76] are concerned.

Lastly, the experimental setup itself may influence contrast and imaging. Here, of particular importance is the used numerical aperture. Using a high numerical aperture (NA) objective lens results in a distribution of k vectors in the excitation field in the focus area. Large NAs (>0.9) will result in light polarization in the focal point that have collinear components with respect to optical axis of the system [77,78]. Therefore, phonons of other symmetries or propagating at oblique angles may be excited even in the bulk area, which was demonstrated by Tuschel on KTP and LN [79]. This may enhance or lower the contrast due to changed selection rules, as signatures of oblique propagating phonons are already

present in the bulk spectra. Stone and Dierolf even used an immersion oil microscope providing a numerical aperture of 1.32 for their system [6].

VIII. CONCLUSION

In this work, we have systematically performed Raman spectroscopy on ferroelectric domain structures in $LiNbO_3$, $LiTaO_3$, and $KTiOPO_4$ as well as atomistic calculations. Here, the goal was to obtain an extensive insight in the mechanism, which alters the Raman spectrum at domain walls and allows for visualization of domain structures. As seen in this work, we have been able to understand the contrast at domain walls by a combination of a macroscopic model, which explains the contrast in terms of relaxed selection rules, and a microscopic model, where local strain and electric fields modify the Raman spectrum. Both effects appear not only to manifest in different spectral responses, but also at different length scales. The observation of largely varying response lengths depending on the method has been first pointed out by Gopalan *et al.* in 2007 [7], where they noted that different analysis methods on domain walls in lithium niobate and tantalate yielded largely different width scales of domain walls. While theory and direct observations of atomic displacements with electron microscopy methods showed the DW transition to be on the order of a few unit cells [17–21], response length around DWs up to the order of several 10 μm have been observed by Bragg topography (resolution a few microns) [28,29]. Many other methods have demonstrated various response length scales in-between, e.g., 1–80 nm with PFM (resolution down to nm; depending on tip radius) [48,80], 500–2000 nm with luminescence, Raman and SHG microscopy (resolution $<$500 nm) [7,49,56,70,74] or refractive index analysis with near-field scanning optical microscopy (NSOM) (resolution $<$100 nm) [50,51]. This work demonstrates this discrepancy to be present in one method, which can be explained in terms of two fundamentally different mechanisms. In the context of the microscopic model, we present a simple atomistic model of strain and electric fields. While our simplified model is able to reproduce the spectral modifications at the domain wall, it certainly does not fully capture the complexity of the real system. Nevertheless, this proposes a path to simulate and understand the domain-wall region on a microscopic scale in LN and LT and a way to close the gap between findings of various response length around DWs [7].

ACKNOWLEDGMENTS

The authors acknowledge the Deutsche Forschungsgemeinschaft (DFG) for financial support by the SFB/TRR 142 through Projects No. B04 and No. B05. The authors thank D. Kool for helpful discussions.

[1] V. Dierolf and C. Sandmann, Appl. Phys. B **78**, 363 (2004).
[2] G. Berth, W. Hahn, V. Wiedemeier, A. Zrenner, S. Sanna, and W. G. Schmidt, Ferroelectrics **420**, 44 (2011).
[3] V. Y. Shur, P. S. Zelenovskiy, M. S. Nebogatikov, D. O. Alikin, M. F. Sarmanova, A. V. Ievlev, E. A. Mingaliev, and D. K. Kuznetsov, J. Appl. Phys. **110** (2011).
[4] M. D. Fontana, R. Hammoum, P. Bourson, S. Margueron, and V. Y. Shur, Ferroelectrics **373**, 26 (2008).
[5] P. Capek, G. Stone, V. Dierolf, C. Althouse, and V. Gopolan, Phys. Status Solidi C **4**, 830 (2007).
[6] G. Stone and V. Dierolf, Opt. Lett. **37**, 1032 (2012).
[7] V. Gopalan, V. Dierolf, and D. A. Scrymgeour, Annu. Rev. Mater. Res. **37**, 449 (2007).
[8] M. Rüsing, C. Eigner, P. Mackwitz, G. Berth, C. Silberhorn, and A. Zrenner, J. Appl. Phys. **119**, 044103 (2016).
[9] Y. Zhang, L. Guilbert, and P. Bourson, Appl. Phys. B **78**, 355 (2004).
[10] V. Ya Shur and P. S. Zelenovskiy, J. Appl. Phys. **116**, 066802 (2014).
[11] V. Ya Shur, D. S. Chezganov, M. S. Nebogatikov, I. S. Baturin, and M. M. Neradovskiy, J. Appl. Phys. **112**, 104113 (2012).
[12] P. S. Zelenovskiy, M. D. Fontana, V. Y. Shur, P. Bourson, and D. K. Kuznetsov, Appl. Phys. A **99**, 741 (2010).
[13] R. Hammoum, M. D. Fontana, P. Bourson, and V. Y. Shur, Ferroelectrics **352**, 106 (2007).
[14] R. Hammoum, M. Fontana, P. Bourson, and V. Shur, Appl. Phys. A **91**, 65 (2008).
[15] Y. Kong, J. Xu, B. Li, S. Chen, Z. Huang, L. Zhang, S. Liu, W. Yan, H. Liu, X. Xie, L. Shi, X. Li, and G. Zhang, Opt. Mater. **27**, 471 (2004).
[16] G. F. Nataf, M. Guennou, A. Haußmann, N. Barrett, and J. Kreisel, Phys. Status Solidi (RRL): Rapid Res. Lett. **10**, 222 (2016).
[17] C.-L. Jia, S.-B. Mi, K. Urban, I. Vrejoiu, M. Alexe, and D. Hesse, Nat. Mater. **7**, 57 (2008).
[18] L. Bursill and P. J. Lin, Ultramicroscopy **18**, 235 (1985).
[19] Y. B. Chen, M. B. Katz, X. Q. Pan, R. R. Das, D. M. Kim, S. H. Baek, and C. B. Eom, Appl. Phys. Lett. **90**, 072907 (2007).
[20] J. Padilla, W. Zhong, and D. Vanderbilt, Phys. Rev. B **53**, R5969(R) (1996).
[21] B. Meyer and D. Vanderbilt, Phys. Rev. B **65**, 104111 (2002).
[22] M. D. Fontana and P. Bourson, Appl. Phys. Rev. **2**, 040602 (2015).
[23] M. Rüsing, S. Sanna, S. Neufeld, G. Berth, W. G. Schmidt, A. Zrenner, H. Yu, Y. Wang, and H. Zhang, Phys. Rev. B **93**, 184305 (2016).
[24] M. R. Tejerina, D. Jaque, and G. A. Torchia, Opt. Mater. **36**, 936 (2014).
[25] M. R. Tejerina, K. Pereira da Silva, A. R. Goñi, and G. A. Torchia, Opt. Mater. **36**, 581 (2013).
[26] M. R. Tejerina, D. Jaque, and G. A. Torchia, J. Appl. Phys. **112**, 123108 (2012).
[27] G. Stone, B. Knorr, V. Gopalan, and V. Dierolf, Phys. Rev. B **84**, 134303 (2011).
[28] T. Jach, S. Kim, V. Gopalan, S. Durbin, and D. Bright, Phys. Rev. B **69**, 064113 (2004).
[29] K. Hassani, M. Sutton, M. Holt, Y. Zuo, and D. Plant, J. Appl. Phys. **104**, 043515 (2008).
[30] D. A. Scrymgeour, V. Gopalan, A. Itagi, A. Saxena, and P. J. Swart, Phys. Rev. B **71**, 184110 (2005).

[31] W. Demtröder, *New York* (Springer, Berlin, 2007), Vol. 4, p. 726
[32] H. Kuzmany, *Solid-State Spectroscopy: An Introduction* (Springer, Berlin, 2009), pp. 1–554.
[33] X. Yang, G. Lan, B. Li, and H. Wang, Phys. Status Solidi B **142**, 287 (1987).
[34] S. Hell, G. Reiner, C. Cremer, and E. H. K. Stelzer, J. Microsc. **169**, 391 (1993).
[35] S. Sanna, S. Neufeld, M. Rüsing, G. Berth, A. Zrenner, and W. G. Schmidt, Phys. Rev. B **91**, 224302 (2015).
[36] M. Rüsing, T. Wecker, G. Berth, D. J. As, and A. Zrenner, Phys. Status Solidi (b) **253**, 778 (2016)
[37] G. E. Kugel, F. Bréhat, B. Wyncket, M. D. Fontana, G. Marnier, C. Carabatos-Nedelec, and J. Mangin, J. Phys. C: Solid State Phys **21**, 5565 (1988).
[38] S. Margueron, A. Bartasyte, A. M. Glazer, E. Simon, J. Hlinka, I. Gregora, and J. Gleize, J. Appl. Phys. **111**, 104105 (2012).
[39] L. Merten, Phys. Status Solidi B **28**, 111 (1968).
[40] R. Claus, J. Brandmüller, G. Borstel, E. Wiesendanger, and L. Steffan, Z. Naturforsch. A **27**, 1187 (1972).
[41] J. Onstott and G. Lucovsky, J. Phys. Chem. Solids **31**, 2171 (1970).
[42] N. Kuroda and Y. Nishina, Solid State Commun. **30**, 95 (1979).
[43] D. Olechna, J. Phys. Chem. Solids **31**, 2755 (1970).
[44] P. Hermet, M. Veithen, and P. Ghosez, J. Phys.: Condens. Matter **19**, 456202 (2007).
[45] V. Ansari, E. Roccia, M. Santandrea, M. Doostdar, C. Eigner, L. Padberg, I. Gianani, M. Sbroscia, J. M. Donohue, L. Mancino, M. Barbieri, and C. Silberhorn, Opt. Express **26**, 2764 (2018).
[46] H. Karlsson and F. Laurell, Appl. Phys. Lett. **71**, 3474 (1997).
[47] S. Sanna, G. Berth, W. Hahn, A. Widhalm, A. Zrenner, and W. G. Schmidt, Ferroelectrics **419**, 1 (2011).
[48] J. Wittborn, C. Canalias, K. V. Rao, R. Clemens, H. Karlsson, and F. Laurell, Appl. Phys. Lett. **80**, 1622 (2002).
[49] V. Dierolf and C. Sandmann, J. Lumin. **125**, 67 (2007).
[50] S. Kim and V. Gopalan, Mater. Sci. Eng. B **120**, 91 (2005).
[51] T. J. Yang, V. Gopalan, P. J. Swart, and U. Mohideen, Phys. Rev. Lett. **82**, 4106 (1999).
[52] N. I. Sorokina and V. I. Voronkova, Crystallogr. Rep. **52**, 80 (2007).
[53] Y.-L. Chen, J.-J. Xu, X.-Z. Zhang, Y.-F. Kong, X.-J. Chen, and G.-Y. Zhang, Appl. Phys. A **74**, 187 (2002).
[54] A. Grisard, E. Lallier, K. Polgar, and A. Peter, Electron. Lett. **36**, 1043 (2000).
[55] K. Kitamura, Y. Furukawa, K. Niwa, V. Gopalan, and T. E. Mitchell, Appl. Phys. Lett. **73**, 3073 (1998).
[56] S. Cherifi-Hertel, H. Bulou, R. Hertel, G. Taupier, K. D. H. Dorkenoo, C. Andreas, J. Guyonnet, I. Gaponenko, K. Gallo, and P. Paruch, Nat. Commun. **8**, 15768 (2017).
[57] J. P. Perdew, K. Burke, and M. Ernzerhof, Phys. Rev. Lett. **77**, 3865 (1996).
[58] M. Ernzerhof and G. E. Scuseria, J. Chem. Phys. **110**, 5029 (1999).
[59] G. Kresse and J. Furthmüller, Comput. Mater. Sci. **6**, 15 (1996).
[60] G. Kresse and J. Furthmüller, Phys. Rev. B **54**, 11169 (1996).
[61] H. Boysen and F. Altorfer, Acta Crystallogr., Sect. B **50**, 405 (1994).
[62] S. Abrahams, E. Buehler, W. Hamilton, and S. Laplaca, J. Phys. Chem. Solids **34**, 521 (1973).
[63] J. Servoin and F. Gervais, Solid State Commun. **31**, 387 (1979).
[64] C. Raptis, Phys. Rev. B **38**, 10007 (1988).
[65] Y. Tezuka, S. Shin, and M. Ishigame, Phys. Rev. B **49**, 9312 (1994).
[66] H. R. Xia, S. Q. Sun, X. F. Cheng, S. M. Dong, H. Y. Xu, L. Gao, and D. L. Cui, J. Appl. Phys. **98**, 033513 (2005).
[67] Y. Li, W. G. Schmidt, and S. Sanna, Phys. Rev. B **91**, 174106 (2015).
[68] K. Nakamura, J. Kurz, K. Parameswaran, and M. M. Fejer, J. Appl. Phys. **91**, 4528 (2002).
[69] V. Gopalan and M. C. Gupta, Ferroelectrics **198**, 49 (1997).
[70] G. Berth, V. Quiring, W. Sohler, and A. Zrenner, Ferroelectrics **352**, 78 (2007).
[71] T. Kämpfe, P. Reichenbach, M. Schröder, A. Haußmann, L. M. Eng, T. Woike, and E. Soergel, Phys. Rev. B **89**, 035314 (2014).
[72] M. Schröder, A. Haußmann, A. Thiessen, E. Soergel, T. Woike, and L. M. Eng, Adv. Funct. Mater. **22**, 3936 (2012).
[73] L. Gui, H. Hu, M. Garcia-Granda, and W. Sohler, Opt. Express **17**, 3923 (2009).
[74] G. Berth, V. Wiedemeier, K.-P. Hüsch, L. Gui, H. Hu, W. Sohler, and A. Zrenner, Ferroelectrics **389**, 132 (2009).
[75] P. Mackwitz, M. Rüsing, G. Berth, A. Widhalm, K. Müller, and A. Zrenner, Appl. Phys. Lett. **108**, 152902 (2016).
[76] L. Chang, Y. Li, N. Volet, L. Wang, J. Peters, and J. E. Bowers, Optica **3**, 531 (2016).
[77] Y. Saito, M. Kobayashi, D. Hiraga, K. Fujita, S. Kawano, N. I. Smith, Y. Inouye, and S. Kawata, J. Raman Spectrosc. **39**, 1643 (2008); L. Vinet and A. Zhedanov, J. Phys. A: Math. Theor. **44**, 085201 (2011).
[78] Y. Saito and P. Verma, J. Phys. Chem. Lett. **3**, 1295 (2012).
[79] D. Tuschel, Spectroscopy **32**, 14 (2017).
[80] D. A. Scrymgeour and V. Gopalan, Phys. Rev. B **72**, 024103 (2005).